Research Square

Preprints are preliminary reports that have not undergone peer review.
They should not be considered conclusive, used to inform clinical practice,
or referenced by the media as validated information.

Annealing-Induced Nanosheet Formation in Sputtered VOx for High-Performance NH3 Sensing

Semih İnceçam

semih.incecam@gazi.edu.tr

Gazi University

Selim Acar

Gazi University

Research Article

Keywords: VOx thin films, Magnetron sputtering, Annealing-induced evolution, Nanosheet structures, NH3 gas sensing, Surface-controlled sensing, Metal oxide sensors

Posted Date: November 20th, 2026

DOI: https://doi.org/10.21203/rs.3.rs-10627169/v1

License: This work is licensed under a Creative Commons Attribution 4.0 International License.
Read Full License

Additional Declarations: No competing interests reported.

Annealing-Induced Nanosheet Formation in Sputtered VOx for High-Performance NH_3 Sensing

Semih İnceçam [1,2] * and Selim Acar[3]

[1] Department of Advanced Technologies, Graduate School of Natural and Applied Sciences, Gazi University, Ankara, Turkey

[2] Roketsan Missiles Inc., 06780 Ankara, Turkey

[3] Department of Physics, Faculty of Science, Gazi University, Ankara, Turkey

*Author to whom any correspondence should be addressed.

Email: semih.incecam@gazi.edu.tr and semih.incecam@roketsan.com.tr

Abstract

This study presents the fabrication and optimization of VOx thin-film Ammonia (NH_3) gas sensors deposited by reactive DC magnetron sputtering, followed by systematic post-annealing in the temperature range of 100–550 °C. Systematic correlations between annealing temperature, phase composition, film morphology, and NH_3 sensing response were established. X-ray diffraction analysis revealed a transition from an amorphous structure to a highly crystalline, preferentially oriented orthorhombic V_2O_5 phase, with the nearly phase-pure, highly crystalline structure obtained at annealing temperatures of 480 °C and above. FESEM observations demonstrated significant morphological evolution, culminating in the formation of porous nanosheet-like structures at 480 °C. Such a morphology is expected to expose more accessible surface sites and facilitate NH_3 diffusion, thereby contributing to the enhanced sensing performance. Gas sensing measurements toward NH_3 showed a strong dependence on annealing temperature, with each sensor exhibiting a distinct optimum operating temperature governed by adsorption–desorption and surface reaction kinetics. Among all samples, the 480 °C annealed sensor exhibited the best performance, achieving a maximum sensitivity of 104% toward 50 ppm NH_3 at an operating temperature of 207 °C, along with fast response–recovery behavior and excellent stability. The enhanced sensing performance is attributed primarily to

the optimized crystallinity, reduced lattice microstrain, and porous nanosheet morphology achieved at the 480 °C annealing condition. Literature-reported V^{5+}/V^{4+} mediated surface redox processes in V_2O_5 may also contribute to the observed NH_3 response. The 460 °C annealed sensor additionally achieves sensitivities of 42% at 67 °C, indicating viable low-power operating conditions. Overall, this work demonstrates that controlled post-annealing is a key strategy for tuning VOx thin-film properties and provides a simple, scalable, and cost-effective approach for the development of high-performance NH_3 gas sensors.

Keywords: VOx thin films, Magnetron sputtering, Annealing-induced evolution, Nanosheet structures, NH_3 gas sensing, Surface-controlled sensing, Metal oxide sensors

1. INTRODUCTION

Ammonia ranks among the highest-volume commodity chemicals worldwide, with broad utility spanning agricultural fertilization, industrial refrigeration, pharmaceutical and fine chemical synthesis, and food production. Despite its economic importance, NH_3 poses acute toxicological and corrosive hazards at concentrations exceeding safe exposure thresholds. Beyond its industrial relevance, NH_3 has gained recognition as a clinically meaningful exhaled breath biomarker: pathologically elevated breath NH_3 levels have been linked to renal insufficiency, hepatic impairment, and specific bacterial infections [1, 2]. In parallel, NH_3 generated by microbial proteolytic activity serves as a reliable spoilage index for protein-rich foodstuffs such as meat and seafood. These diverse and critical application scenarios collectively underscore the pressing need for NH_3 detection platforms that simultaneously deliver high sensitivity, good selectivity, reliable long-term stability, and low manufacturing cost, for deployment in environmental surveillance, occupational safety, clinical breath analysis, and food freshness monitoring [1, 2, 3].

Among the available gas detection platforms, chemiresistive sensors based on metal oxide semiconductors (MOS) have emerged as a leading technology owing to their uncomplicated transducer geometry, cost-effective fabrication, compatibility with device miniaturization, and capability for rapid and sensitive detection [4]. A broad range of semiconducting oxides has been explored for this purpose, including n-type candidates such as SnO_2 [5], ZnO [6], TiO_2 [7], WO_3 [8], and In_2O_3 [9], as well as MoO_3 [10] and the p-type material CuO [11]. These two classes exhibit contrasting conduction mechanisms, n-type oxides show resistance decrease when reducing gases donate electrons to the conduction band, whereas p-type materials follow the opposite trend through majority carrier depletion at grain boundaries (enabling complementary sensing strategies across a wide analyte range). In both cases, detection performance is tightly coupled to crystallographic order, surface chemistry, microstructural morphology, defect concentration, and adsorption–desorption dynamics. Nanostructure engineering (yielding morphologies such as nanorods, nanowires, nanofibers, hierarchical nanoflowers, porous films, and two-dimensional nanosheets) has therefore been widely pursued to maximize the surface-to-volume ratio, increase the density of reactive surface sites, and promote rapid analyte diffusion, all of which directly benefit detection performance [1, 12, 13].

Among the various transition metal oxides, vanadium pentoxide (V_2O_5) is an attractive sensing material owing to its layered orthorhombic crystal structure, multiple oxidation states, high catalytic activity, excellent chemical stability, and favorable electronic properties. V_2O_5 is generally considered an n-type semiconductor with a bandgap in the range of 2.2–2.8 eV. Its multivalent vanadium states (V^{5+}/V^{4+}) and oxygen-deficient structure enable efficient charge transfer processes and surface redox reactions during gas adsorption [14, 15]. Furthermore, the layered structure of V_2O_5 facilitates ion diffusion and surface interactions, which benefit gas sensing. Different V_2O_5 nanostructures including nanoparticles, nanowires, nanorods,

nanofibers, nanosheets, and thin films have been investigated for detecting gases such as NH_3, NOx, ethanol, hydrogen, and volatile organic compounds. In particular, porous nanosheet-like morphologies have demonstrated enhanced sensing behavior due to their high accessible adsorption sites and improved gas diffusion characteristics [1, 14]. Among these nanostructures, porous nanosheets are particularly attractive because their open architecture facilitates rapid analyte diffusion while maintaining abundant accessible adsorption sites, making them highly suitable for chemiresistive gas sensing. The Lewis acid character of V^{5+} surface sites further favors NH_3 detection: the lone electron pair of NH_3 coordinates directly with V^{5+} centers, driving efficient charge transfer and a strong chemiresistive response at moderate temperatures [15, 16].

Efforts to improve V_2O_5 sensing performance have targeted morphology engineering, noble metal sensitization, heterostructure formation, and light-assisted activation. Room-temperature NH_3 sensing based on porous V_2O_5 nanosheets has been reported, where the enhanced sensing performance was attributed to the high porosity and increased surface-active sites of nanosheet architectures [1]. Reactive DC magnetron sputtering studies have demonstrated that oxygen partial pressure during deposition governs the stoichiometry and electrical properties of vanadium oxide thin films [17]; complementarily, postdeposition annealing atmosphere and temperature provide a further route to controlling phase composition and stability [18]. Furthermore, recent studies investigating annealing effects on vanadium oxide nanostructures show that thermal treatment governs crystallinity, grain growth, oxygen vacancy concentration, and morphology evolution [14]. Elevated annealing temperatures facilitate oxygen diffusion and recrystallization processes, resulting in improved crystal quality and the emergence of sheet-like morphologies with enhanced surface activity [14].

However, most studies have examined structural evolution and sensing characteristics in isolation. To the best of our knowledge, a systematic investigation combining wide-range

annealing, fine-temperature mapping (460–490 °C), phase evolution, nanosheet formation, and NH_3 sensing optimization in sputtered VOx thin films has not been reported. In particular, the mechanistic links between amorphous-to-crystalline phase transformation, nanosheet formation, and chemiresistive response remain incompletely mapped [14, 17].

In this study, VOx thin films were deposited by reactive DC magnetron sputtering and subsequently annealed at different temperatures to systematically investigate the influence of annealing temperature on phase composition, film morphology, and NH_3 sensing response. Structural analyses revealed a progressive transformation from amorphous VOx toward mixed vanadium oxide phases and nearly phase-pure orthorhombic V_2O_5 with increasing annealing temperature. Simultaneously, remarkable morphology evolution toward porous nanosheet-like structures was observed, accompanied by enhanced crystallinity and modified characteristics. The correlation between annealing-driven structural evolution and gas sensing behavior was comprehensively investigated through XRD, FESEM, and gas sensing analyses. The obtained results demonstrate that thermally engineered phase purification and nanosheet morphology evolution play a critical role in enhancing NH_3 sensing performance, providing valuable insight into structure–property relationships in sputtered vanadium oxide sensing materials.

2. EXPERIMENTAL

P-type boron-doped silicon wafers (4-inch diameter, <100> orientation, 5–10 Ω·cm resistivity, 525 μm thickness, single-side polished) were used as substrates. Prior to deposition, the substrates were ultrasonically cleaned in 99.5% acetone for 10 min, followed by 99.8% isopropyl alcohol for 10 min, to remove organic contaminants and surface residues. The cleaned substrates were then dried under a stream of 99.99% purity nitrogen gas and loaded into the substrate holder of the sputtering system.

The DC facing-target magnetron sputtering system was used to deposit the V thin films on the cleaned silicon substrates by using a circular vanadium target of 4-inch in diameter supplied by Kurt J Lesker with a purity of 99.99%. The sputtering conditions for VOx films and Ti/Au electrodes are shown in Table 1 and Table 2.

The deposited thin films were annealed in air for 1 h at temperatures of 100, 200, 300, 400, 450, 500, and 550 °C. Initial FESEM observations revealed the emergence of nanosheet-like structures within the 450–500 °C temperature range. Therefore, additional annealing temperatures of 460, 470, 480, and 490 °C were intentionally included to systematically resolve the structural transition. After each annealing step, FESEM images and XRD patterns were acquired. Sensors are designated according to their annealing temperature (e.g., VO_100 for the 100 °C sample); the as-deposited, unannealed sensor is denoted VO_AG.

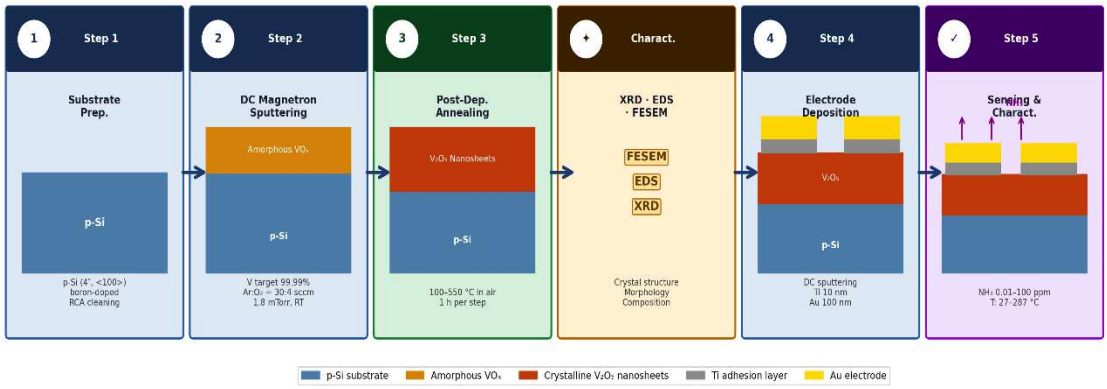


Figure 1. Schematic overview of the complete fabrication and characterisation process flow for VOx thin-film NH_3 gas sensors. Step 1: substrate preparation (p-Si wafer cleaning). Step 2: reactive DC magnetron sputtering of VOx. Step 3: systematic post-deposition annealing (100–550 °C) with a fine-scan step in the 460–490 °C range. Step 4: Ti/Au electrode deposition by DC sputtering. Step 5: Characterisation (FESEM, EDS, XRD) and gas sensing.

Table 1. Optimized sputtering parameters for vanadium oxide film deposition.

Parameters	**Values**
Target	Vanadium (99.99%)
Temperature	Room Temperature

Working Pressure	1.8 mTorr
Reactive Gas	99.99% O2
Gas Flow (Ar:O_2)	30:4
Power	550W (DC)
Deposition Time	20min

Table 2. Optimized sputtering parameters for Ti/Au electrodes deposition.

Parameters	**Values (1)**	**Values (2)**
Target	Ti (99.99%)	Au (99.99%)
Temperature	Room Temperature	Room Temperature
Working Pressure	2.7 mTorr	2.7 mTorr
Reactive Gas	-	-
Gas Flow (Ar:O_2)	30:0	30:0
Power	300W (DC)	350W (DC)
Deposition Time	5.5min	3min

The surface morphology of the vanadium oxide thin films was examined by field-emission scanning electron microscopy (FESEM, Hitachi S-4800). X-ray diffraction (XRD, RIGAKU Ultima IV, Cu Kα radiation) analysis demonstrates the crystallographic structure of the thin films. Surface characterization processes were performed after annealing. Following surface characterization, interdigital contacts were coated. Accordingly, the gas sensing properties of the annealed thin films were evaluated after electrode fabrication (Fig. 2).

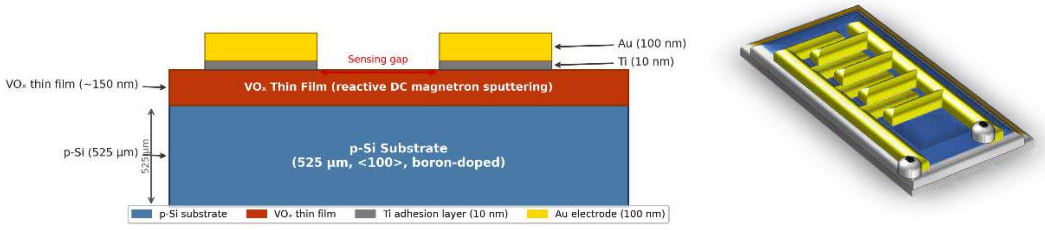


Figure 2. The schematic diagram of the sensor.

Gas sensing measurements of the VOx thin-film sensors were performed in a dynamic flow system comprising a test chamber, an electronically controlled gas valve, a flat heating plate, a temperature controller (Lakeshore 525), two mass flow controllers (MFCs -ALICAT) to regulate gas mixing and flow, a source-measure unit (Keithley 2400), and an automated data acquisition system. A schematic diagram of the gas sensing test system is shown in Fig. 3.

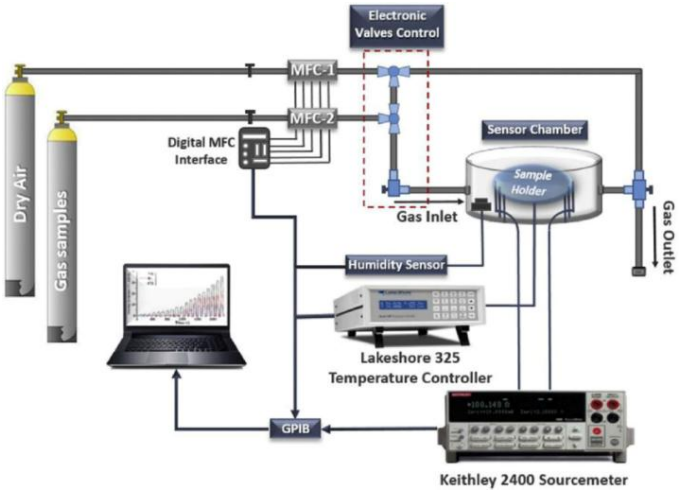


Figure 3. The device of gas sensing test system.

Operating temperature is a decisive variable in chemiresistive MOS sensing, as it simultaneously governs the activation energy available for gas–surface reactions, the adsorption–desorption equilibrium, and charge carrier mobility within the oxide layer. Below the optimum, insufficient thermal energy suppresses reactive surface interactions, yielding a diminished signal output. Progressive heating accelerates reaction kinetics and improves the measured response until a peak is reached; further temperature increases cause desorption to outpace adsorption, reducing analyte residence time on the surface and lowering sensitivity. High operating temperatures additionally impose greater power demands and may accelerate microstructural degradation of the active layer. Determination of the temperature of maximum

response therefore represents a fundamental optimization step, defining the operating point that best balances sensing performance, operating temperature, and long-term reliability.

In order to determine the gas detection properties of the produced gas sensors, it is necessary to first determine the optimal operating temperature. Therefore, to determine the optimal operating temperature, gas detection measurements were carried out in 20 ℃ steps in the temperature range of 27–287℃, at a gas concentration of 50 ppm NH_3. Before starting the measurements, dry air was sent into the cell to stabilize the sensor and the chamber. The flow rate of dry air was kept constant throughout the experiment to observe its behavior at different concentrations under identical conditions.

3. RESULT & DISCUSSION

FESEM analyses clearly reveal that post-deposition annealing has a pronounced effect on the surface morphology of the VOx thin films. The as-deposited film exhibits a relatively smooth, compact, and featureless surface, which is expected to provide fewer accessible adsorption sites for NH_3 molecules. As the annealing temperature increases, the surface progressively evolves into a rougher and more porous nanosheet-like architecture, providing more exposed adsorption sites and facilitating gas diffusion. At higher annealing temperatures, particularly around 480 °C and above, the morphology is dominated by well-developed nanosheet-like architectures with a porous and interconnected network. The porous nanosheet morphology provides an open surface architecture with abundant accessible adsorption sites and efficient gas-diffusion pathways, thereby promoting NH_3 adsorption and surface reaction kinetics. Consequently, these morphological features are expected to contribute significantly to the enhanced NH_3 sensing characteristics of the optimally annealed samples. The observed morphological evolution is consistent with thermally activated grain growth and surface diffusion processes, which promote the formation of energetically favorable nanosheet

structures at elevated temperatures. These structural characteristics are expected to influence the adsorption, diffusion, and charge-transfer processes during gas sensing. Their impact on the NH_3 sensing performance is discussed in the following section.

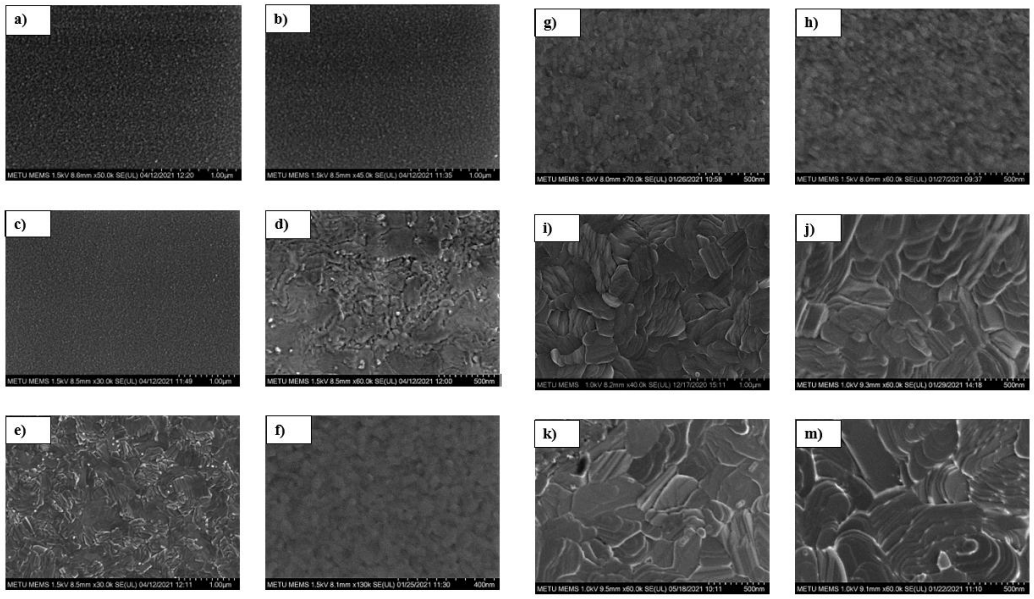


Figure 4. FESEM images for sensors;
a) VO_AG b) VO_100 c) VO_200 d) VO_300 e) VO_400 f) VO_450 g) VO_460 h) VO_470 i) VO_480 j) VO_490 k) VO_500 m) VO_550

The elemental composition and surface morphology of the VOx thin films were systematically investigated using EDS and FESEM analyses in order to understand the effect of post-deposition annealing on the material properties. The EDS spectra confirm the successful formation of vanadium oxide thin films without detectable contamination. The characteristic peaks corresponding to V and O are clearly observed, while the Si signal originates from the underlying silicon substrate. No impurity-related peaks are detected within the sensitivity limits of the technique, indicating high film purity and well-controlled sputtering conditions. These findings are consistent with the intended deposition process and verify the formation of VOx thin films. However, considering the surface-sensitive and semi-quantitative nature of EDS analysis, the results mainly provide confirmation of elemental presence rather than precise stoichiometric composition.

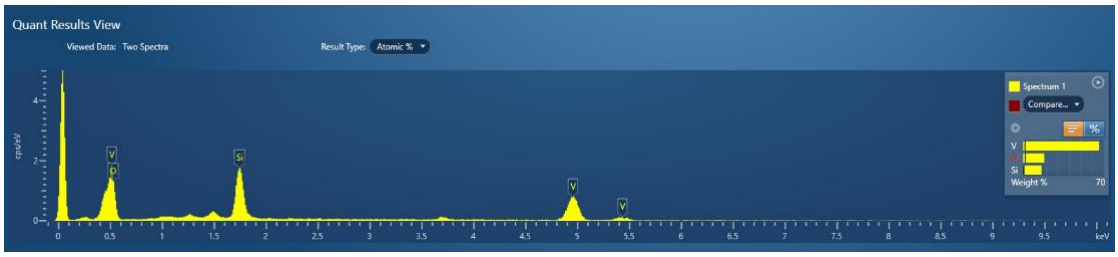


Figure 5. EDS spectra

The crystal structure of the VOx thin films and its evolution with annealing temperature were investigated by X-ray diffraction (XRD). The XRD patterns reveal a pronounced dependence of crystallization behavior on annealing temperature. The as-grown and low-temperature-annealed samples (≤200 °C) exhibit broad and weak diffraction features, indicating a predominantly amorphous or poorly crystalline structure. With increasing annealing temperature, distinct diffraction peaks begin to emerge at temperatures ≥300 °C, indicating the onset of crystallization. In this intermediate temperature range (300–400 °C), a mixed-phase structure consisting of V_3O_7 (ICDD: 01-071-0454) and orthorhombic V_2O_5 (ICDD: 01-075-0457) is observed. Further increase in annealing temperature leads to the formation of a well-crystallized and nearly phase-pure orthorhombic V_2O_5 structure at 480 °C and above, whereas the samples annealed at 450–470 °C exhibit comparatively weak diffraction intensities, indicating that long-range crystalline order is still developing within this transition range. The dominant diffraction peak located at $2\theta \approx 20.35°$, corresponding to the (010) plane of V_2O_5, indicates a preferential orientation along the b-axis. The indexing follows the ICDD 01-075-0457 setting, in which b is the layer-stacking axis; the same reflection corresponds to (001) in the alternative setting where c denotes the stacking axis. In addition, the progressive sharpening and intensification of the diffraction peaks with increasing annealing temperature suggest significant grain growth, reduction in microstrain, and improved crystallinity. These structural

improvements are expected to facilitate charge transfer during the gas-sensing process, thereby contributing to the enhanced sensing performance.

Bragg's law was applied to the XRD patterns to extract the lattice parameters a, b, and c. The unit cell volume was subsequently calculated from these parameters. The derived values and unit cell volumes are compiled in Table 3.

Table 3. Calculated lattice parameters (a, b, c) and unit-cell volumes of the crystalline sensors, compared with the reference V_2O_5 card (ICDD: 01-075-0457).

Sensor	Lattice parameter a (Å)	Lattice parameter b (Å)	Lattice parameter c (Å)	Volume V (Å^3)
VO_300	11.30	4.26	3.51	168.964
VO_400	11.30	4.31	3.56	173.383
VO_450	11.95	3.82	3.56	162.510
VO_460	10.82	4.38	3.44	163.027
VO_470	11.05	4.41	3.56	173.724
VO_480	11.48	4.38	3.55	178.502
VO_490	11.51	4.40	3.44	174.215
VO_500	11.53	4.40	3.41	172.996
VO_550	11.58	4.45	3.20	164.899
V_2O_5 (ICDD: 01-075-0457)	11.48	4.36	3.55	177.938

The obtained lattice parameters show deviations when compared with the reference V_2O_5 card (ICDD: 01-075-0457), which has orthorhombic symmetry with a = 11.48 Å, b = 4.36 Å and c = 3.55 Å (space group Pmn21, No. 31; $\alpha = \beta = \gamma = 90°$). For most samples the calculated unit-cell volumes (162–174 Å^3) are smaller than the reference value of 177.94 Å^3, indicating a slight lattice contraction which may be associated with lattice microstrain rather than an expansion.

The largest deviations are observed for the weakly crystalline VO_450 and VO_460 samples, for which the parameter determination from a limited number of broad reflections carries a correspondingly larger uncertainty. No monotonic trend of the unit-cell volume with annealing temperature is observed. Among the investigated samples, VO_480 exhibits lattice parameters that are in the closest agreement with the reference orthorhombic V_2O_5 structure, with only a minor deviation observed for the b lattice parameter.

In addition to phase identification and lattice parameter determination, the estimation of crystallite size is of great importance for nanostructured gas sensor materials. Smaller crystallite sizes combined with increased surface roughness are known to enhance gas sensing performance by increasing the density of active sites and promoting surface reactions. Therefore, the interplay between crystallite size, lattice strain, and gas sensing characteristics is a critical factor in understanding and optimizing the performance of VOx-based gas sensors. For this purpose, various studies were carried out to investigate the relationship between crystallite size, internal microstrain, and gas sensing properties in detail.

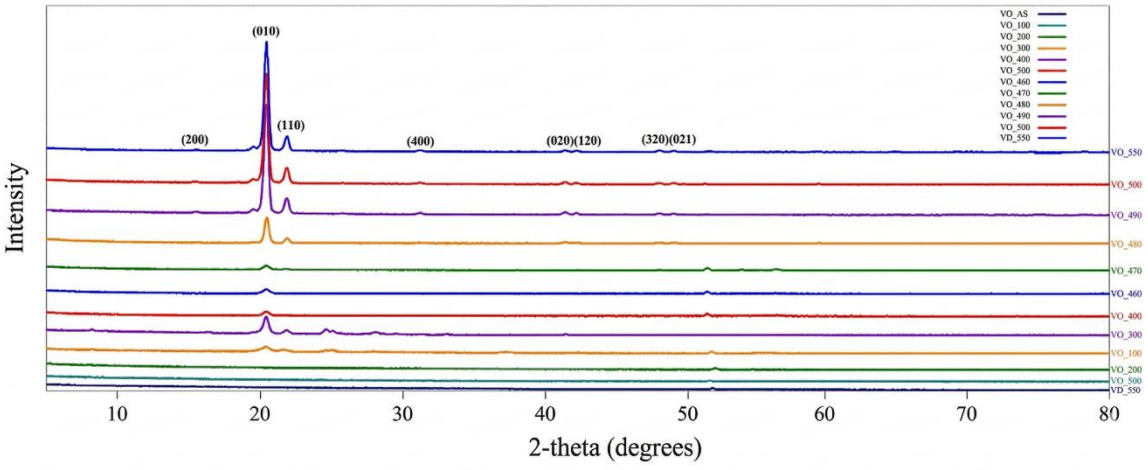


Figure 6. XRD patterns of the sensors annealed at different temperatures. The indexed reflections belong to orthorhombic V_2O_5 (ICDD: 01-075-0457)

The X-ray diffraction peak broadens in nanocrystals due to crystal size and intrinsic stress effects, and this peak broadening normally consists of two parts: physical broadening and instrumental broadening. This broadening can be corrected using the following equation;

$$\beta_d^2 = \beta_m^2 - \beta_i^2$$

In the equation, βm represents the measured peak broadening, βi the instrumental broadening, and βd the corrected (physical) broadening. In this study, position calibration was performed on the obtained data using a standard reference of crystalline silicon, and the instrumental broadening was calculated. Half-width (FWHM) calculations were made for each peak by measuring the instrumental broadening and physical broadening. The average crystallite size was calculated using the Scherrer equation with the corrected (physical) broadening. From the Scherrer equation given below, the average crystallite size of the deposited thin films was calculated.

$$D = \frac{0{,}94\lambda}{\beta_d cos\theta}$$

In this equation, D represents the crystallite size; λ, the X-ray wavelength (Cu Kα, λ = 1.5406 Å); βd, the corrected full width at half maximum (in radians); and θ, the Bragg angle of the peak maximum.

The crystallite size (D) for the sensors was determined using the Scherrer formula from the width at half the height (FWHM) of the (010) XRD reflection. Additionally, the average crystallite size was calculated by determining the crystallite size for all peaks using the Scherrer method. The internal microstrain is calculated from the corrected peak broadening using a separate relation.

Using the equation given below, the internal microstrain was calculated for the (010) reflection and, additionally, as an average over all diffraction peaks.

$$\varepsilon = \frac{\beta_d}{4tan\theta}$$

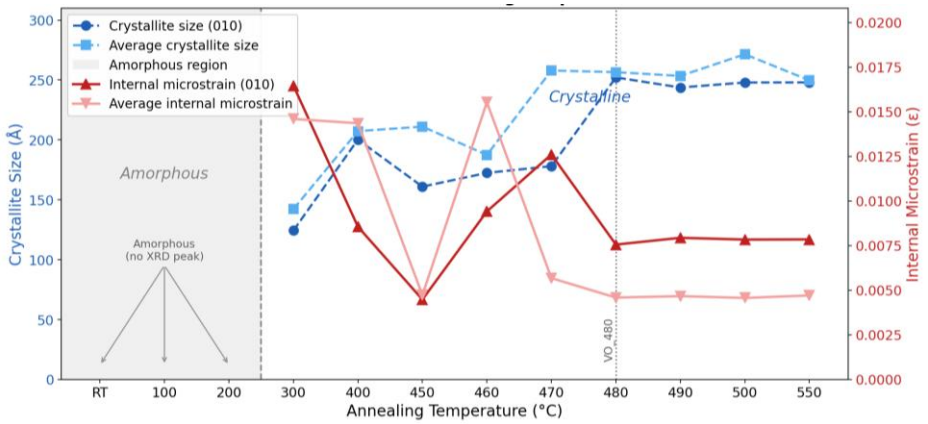


Fig. 7. Crystallite size (left axis) and average internal microstrain (right axis) as a function of annealing temperature. The vertical dashed line marks the 480 °C condition corresponding to maximum sensing performance.

Table 4. Crystallite sizes obtained by the Scherrer method and internal microstrain values of the sensors exhibiting crystalline properties, calculated from the corrected XRD peak broadening.

Sensor	Crystallite size (010) (Å)	Average Crystallite size (Å)	Internal microstrain (ε) (010)	Average internal microstrain (ε)
VO_300	124.30	142.12	0.01646	0.01459
VO_400	200.20	207.28	0.00855	0.01435
VO_450	160.93	211.03	0.00447	0.00472
VO_460	172.40	187.42	0.00941	0.01553
VO_470	178.04	257.91	0.01260	0.00567
VO_480	252.11	256.53	0.00755	0.00458
VO_490	243.73	253.39	0.00793	0.00466
VO_500	247.88	271.48	0.00783	0.00456
VO_550	247.97	249.70	0.00784	0.00470

The crystallite size calculated from the (010) reflection varies between 124 Å and 252 Å, while the peak-averaged crystallite size ranges from 142 Å to 271 Å (Table 4). Increasing the annealing temperature promotes crystallization: the crystallite size calculated from the (010) reflection increases up to 480 °C and then remains nearly constant, while the average lattice microstrain decreases from approximately 0.0146 at 300 °C to about 0.0046 for the samples annealed at 480 °C and above (Fig. 7). These observations are consistent with thermally

activated grain growth accompanied by progressive lattice relaxation during annealing, indicating an overall improvement in the structural quality of the VOx films.

The structural and morphological evolution from amorphous VOx to crystalline V_2O_5 nanosheets is a thermally activated process governed by atomic diffusion and surface kinetics. At low annealing temperatures (≤ 200 °C), the available thermal energy is insufficient to induce long-range atomic rearrangement, resulting in a predominantly amorphous or poorly ordered structure. As the annealing temperature increases above 300 °C, enhanced atomic mobility promotes nucleation and growth of crystalline phases, leading to the formation of mixed V_3O_7 and V_2O_5 structures. With further temperature increase, the system tends toward thermodynamically stable orthorhombic V_2O_5.

At the optimum annealing temperature of 480 °C, surface diffusion is expected to become increasingly important and favor anisotropic growth, resulting in the formation of well-defined two-dimensional nanosheet structures rather than dense grain coalescence. This morphological transition is accompanied by the reduced lattice microstrain revealed by XRD and the formation of abundant accessible adsorption sites. Together, these structural characteristics provide favorable conditions for NH_3 adsorption, gas diffusion, and surface reaction processes.

The gas sensing performance of the VOx-based sensors toward NH_3 was systematically investigated to determine their optimum operating temperatures and concentration-dependent response characteristics. In order to identify the optimum operating temperature, gas sensing measurements were carried out in the temperature range of 27–287 °C with 20 °C intervals under a constant NH_3 concentration of 50 ppm. Prior to each measurement, dry air was introduced into the test chamber to stabilize the sensor response, and the air flow rate was kept constant to ensure consistent experimental conditions. Each sensing measurement was repeated three times fabricated sensors, and the reported values represent the average response.

The sensor response was calculated using the relation

$$S = \frac{R_a - R_g}{R_a} \times 100$$

where Ra and Rg represent the electrical resistance of the sensor in air and in the presence of NH_3 gas, respectively. The temperature-dependent sensitivity curves reveal that each sensor exhibits a distinct optimum operating temperature at which the response toward NH_3 is maximized. This behavior is attributed to the temperature-dependent balance between gas adsorption, desorption, and surface reaction kinetics. At low temperatures, insufficient thermal energy limits gas adsorption and surface reactions, whereas at excessively high temperatures, rapid desorption reduces the interaction time between NH_3 molecules and the sensor surface. Therefore, an intermediate operating temperature provides the most favorable balance between NH_3 adsorption, surface reaction, and desorption, resulting in the maximum sensing response. The optimum sensing performance is therefore governed by the synergistic interplay between the annealing-induced structural evolution of the sensing layer and the surface reaction kinetics during NH_3 detection.

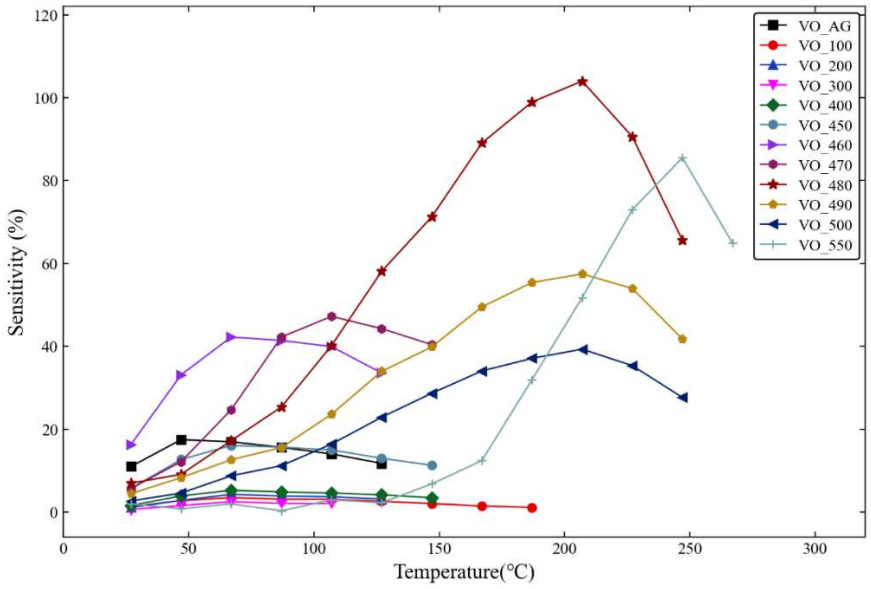


Figure 8. The sensitivity-operating temperature graph of the sensors obtained at a gas concentration of 50 ppm NH_3 between temperatures of 27°C and 287°C.

Among all samples, the VO_480 sensor exhibits the highest sensing performance, achieving a maximum sensitivity of 104% toward 50 ppm NH_3 at an operating temperature of 207 °C. This superior performance is associated with the well-crystallized orthorhombic V_2O_5 phase and the porous nanosheet morphology revealed by XRD and FESEM, respectively. Together, these structural characteristics provide abundant accessible adsorption sites and favorable pathways for charge transfer during gas sensing.

In addition to VO_480, the VO_470 and VO_460 sensors also demonstrate enhanced sensing responses, with sensitivities reaching approximately 47% and 42%, respectively. Notably, the VO_460 sensor exhibits relatively high sensitivities (~42%) at a significantly lower operating temperature of 67 °C. Low-temperature operation at 67 °C reduces heater power requirements, VO_460 thus provides a lower-temperature alternative when a sensitivity of approximately 42% at 50 ppm is acceptable. It is also noteworthy that VO_460 achieves this high response despite its comparatively weak XRD crystallinity, suggesting that the emerging nanosheet-like surface morphology is an important contributing factor to the enhanced sensing performance, in addition to crystallinity.

After determining the optimum operating temperature for each sensor, dynamic gas sensing measurements were conducted over a wide NH_3 concentration range from 0.01 ppm to 100 ppm. The results, summarized in Table 5 and Fig.10, show that the sensor response increases with increasing gas concentration for all samples. However, the sensitivity tends to saturate beyond 50 ppm, and in some cases, a slight decrease is observed at higher concentrations. This saturation reflects the finite density of active adsorption sites on the sensing surface. Similar observations have been reported in the literature, such as the study by M. Hijazi et al. [19], where saturation effects were linked to surface coverage limitations. Interestingly, the VO_500

sensor shows the highest response at the lowest tested concentration (18.90% at 0.01 ppm) yet a comparatively flat concentration dependence up to 50 ppm (39.30%), suggesting early saturation of its accessible adsorption sites, in contrast to the steep log-linear behavior of VO_480. The minimum concentration tested in this work was 0.01 ppm (10 ppb), at which the VO_480 sensor delivered a clearly measurable response of 10.78%, indicating a clear measurable response at the lowest experimentally tested concentration (10 ppb). A quantitative determination of the limit of detection is presented in the following section.

To quantify the analytical detection limit of the VO_480 sensor, a calibration approach based on the measured sensitivity–concentration relationship was applied. Fig. 9 presents the sensitivity of the VO_480 sensor at its optimum operating temperature of 207 °C as a function of NH_3 concentration on a semi-logarithmic scale, spanning the experimentally tested range of 0.01–100 ppm. Two distinct response regimes are apparent: a log-linear region at low concentrations (0.01–5 ppm) amenable to linear calibration and a super-linear saturation region above 10 ppm reflecting progressive occupation of available surface sites.

In the concentration range of 0.01–5 ppm, the sensor displays a well-defined log-linear sensitivity response described by the empirical relationship:

$$S\ (\%) = 9.06 \cdot \log_{10}(C) + 27.95 \quad (R^2 = 0.997)$$

where C is the NH_3 concentration in ppm. The linear dynamic range (LDR) of the sensor extends from 0.01 to 5 ppm with $R^2 = 0.997$, confirming an excellent log-linear calibration fit. The LOD was estimated using the standard signal-to-noise criterion, $LOD = 3\sigma / m$, where σ is the standard deviation of the baseline resistance noise and m = 9.06 %/decade is the slope of the log-linear calibration curve.

Following conventional analytical practice, a baseline noise value of σ = 0.5%, (representative of chemiresistive metal oxide sensors operating under steady-state dry-air conditions) was considered [14]. Because the calibration follows a logarithmic response, $S\ (\%) = 9.06 \cdot \log_{10}(C) + 27.95$, a conventional LOD = 3σ/m extrapolation is not mathematically well-defined for concentrations approaching zero, and the baseline noise value was not experimentally measured for the fabricated device. Therefore, rather than reporting an extrapolated ppb-level LOD, we conservatively state the experimentally verified detection limit, the sensor exhibited a clear and reproducible response of 10.78% at the lowest tested concentration of 10 ppb, indicating a practical detection capability at or below this level. Determination of the exact LOD through direct baseline-noise measurement and sub-ppb testing is identified as future work.

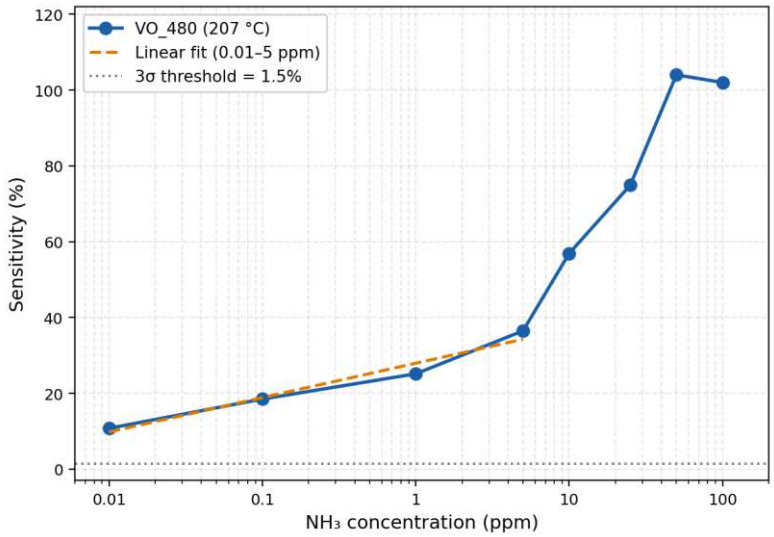


Figure 9. Semi-logarithmic sensitivity–concentration calibration plot for the VO_480 sensor at its optimum operating temperature (207 °C). Data points span the tested range of 0.01–100 ppm NH_3. The orange dashed line is the log-linear regression fit in the 0.01–5 ppm range (R^2 = 0.997)

The strong measurable response observed at the lowest experimentally tested concentration (10 ppb) is consistent with the optimized structure of the VO_480 sensor and may be attributed to the synergistic contribution of three factors: (i) the annealing-induced porous V_2O_5 nanosheet

architecture, which provides abundant accessible adsorption sites for NH_3 molecules; (ii) the improved crystallinity and reduced lattice microstrain achieved after annealing at 480 °C, which facilitate efficient charge transport during sensing; and (iii) literature-reported V^{5+}/V^{4+} mixed-valence surface redox processes in air-annealed V_2O_5, which may further promote electron transfer during NH_3 adsorption and oxidation [14–16]. Together, these factors provide a reasonable explanation for the excellent low-concentration sensing performance observed in the present study. Experimental verification of the sub-ppb detection limit through direct baseline-noise measurements and lower-concentration gas testing remains an important subject for future work.

Table 5. Sensitivities obtained from dynamic measurements at optimum operating temperatures between 0.01 ppm and 100 ppm NH_3 gas concentrations.

Sensor	optimal operating temperat	0.01 ppm Sensitivity (%)	0.1 ppm Sensitivity (%)	1 ppm Sensitivity (%)	5 ppm Sensitivity (%)	10 ppm Sensitivity (%)	25 ppm Sensitivity (%)	50 ppm Sensitivity (%)	100 ppm Sensitivity (%)
VO_AG	47°C	3.86	6.41	7.86	7.92	8.13	10.11	17.45	17.17
VO_100	67°C	0.68	1.22	1.54	1.59	1.64	1.95	3.48	3.40
VO_200	67°C	0.07	0.78	2.13	3.02	3.94	3.93	4.25	4.12
VO_300	67°C	0.02	0.99	1.20	1.60	1.65	1.78	2.46	2.60
VO_400	67°C	1.58	2.03	2.33	2.67	3.05	3.63	5.23	5.17
VO_450	67°C	1.05	4.48	4.31	7.26	7.16	10.77	16.05	15.37
VO_460	67°C	5.24	9.14	17.68	19.23	25.55	31.78	42.23	40.82
VO_470	107°C	8.14	9.03	12.43	14.87	19.42	26.08	47.22	46.90
VO_480	207°C	10.78	18.50	25.16	36.49	56.92	74.90	104.01	101.99
VO_490	207°C	10.50	18.34	22.30	31.22	40.05	46.56	57.46	56.88
VO_500	207°C	18.90	21.04	23.51	27.61	30.44	35.53	39.30	39.10
VO_550	247°C	4.29	9.48	14.90	24.32	24.21	33.30	85.52	82.94

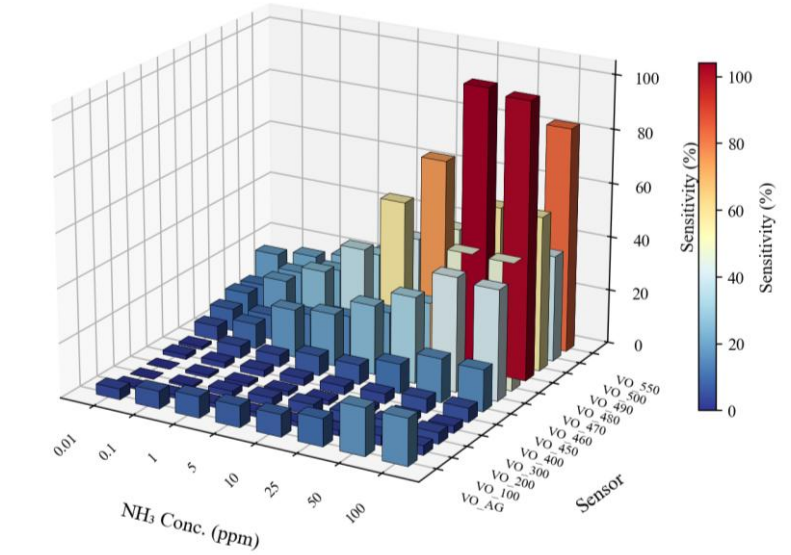


Fig. 10. Three-dimensional bar-chart representation of the sensitivity data listed in Table 5: sensitivity of all twelve VOx sensors as a function of NH_3 concentration (0.01–100 ppm), each measured at its respective optimum operating temperature. Bar height and color both scale with sensitivity (%).

The dynamic response characteristics of the VO_480 sensor further confirm its superior sensing behavior (Fig.11). The sensor exhibits clear and repeatable response–recovery cycles with increasing NH_3 concentrations, indicating good stability and reversibility. The stepwise increase in sensitivity with concentration demonstrates reliable detection capability over a broad concentration range. Overall, the enhanced NH_3 sensing performance of the VOx sensors, particularly for the VO_480 sample, can be attributed to the synergistic effect of improved crystallinity, optimized lattice structure, and annealing-induced nanosheet morphology. These factors collectively enhance gas adsorption, surface reaction kinetics, and charge transfer processes, resulting in superior sensing performance.

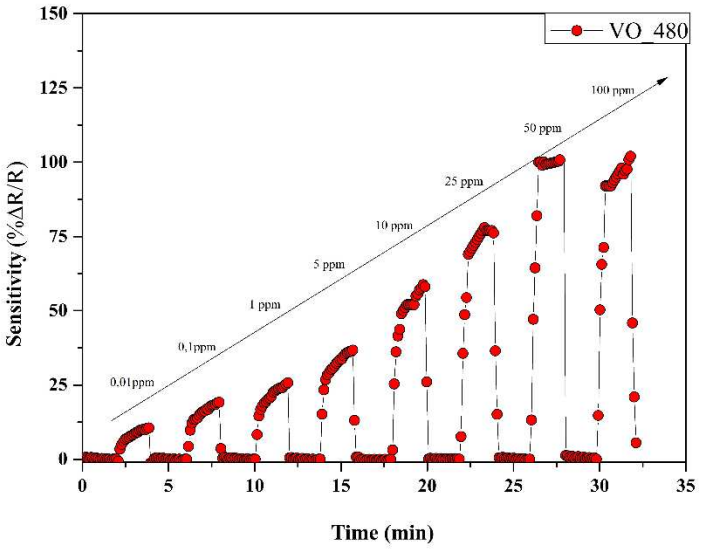


Figure 11. VO_480 dynamic gas measurement result

Transient kinetic metrics (specifically response time and recovery time) are among the most practically informative figures of merit for chemiresistive sensors, since they determine how rapidly a device can track a concentration change and subsequently return to a baseline-ready state for continuous monitoring. The transient performance of the VO_480 sensor was characterized by recording the resistance variation during successive NH_3 exposure and purge cycles, as shown in Figure 12(a). Response time (Tres) was taken as the duration required for the sensor signal to complete 90% of its total excursion following gas introduction; recovery time (Trec) was correspondingly defined as the duration required to return to within 10% of the pre-exposure baseline after gas removal. As illustrated in the figure, the VO_480 sensor exhibits a rapid response time of approximately 46 s and a recovery time of about 28 s, indicating fast adsorption and desorption kinetics. The sharp increase and decrease in sensitivity during gas on/off cycles demonstrate excellent reversibility and stability of the sensor. This fast dynamic behavior can be attributed to the porous nanosheet-like morphology and high surface-to-volume ratio of the VO_480 sample, which facilitate efficient diffusion of

NH_3 molecules and rapid surface reactions. Furthermore, the improved crystallinity, as confirmed by XRD analysis, contributes to enhanced charge transport and faster sensor response. It is further noted that the recovery is faster than the response, this atypical behavior for chemiresistive MOS sensors can be rationalized by the open, porous nanosheet network, which permits rapid purging of the analyte under the constant-flow conditions employed.

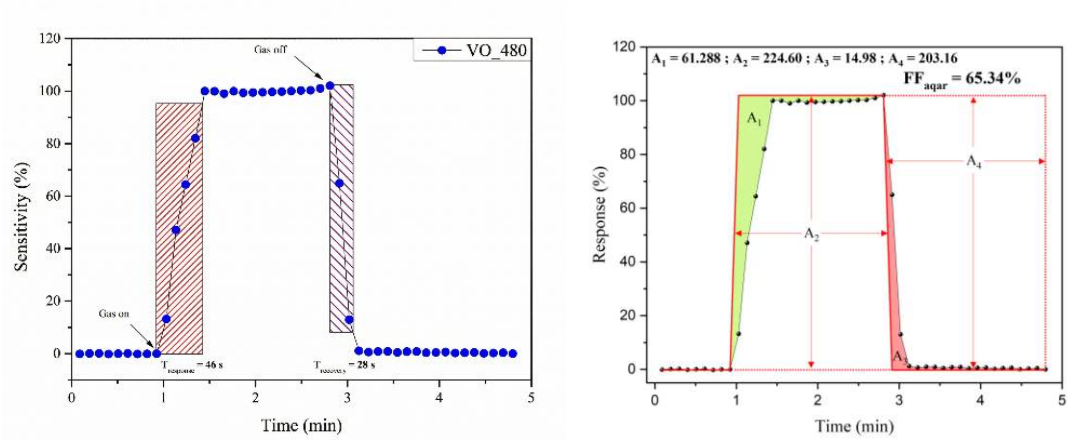


Figure 12. a) The response and b) its application on the signal of the VO_480 sensor to 50 ppm ammonia gas at the optimal working temperature of 207 °C.

To provide an additional assessment of the dynamic sensing characteristics, the fill factor (FF) concept previously introduced by our group for chemiresistive gas sensors was also applied to the response curve of the optimized VO_480 sensor [20]. Originally adapted from the fill factor used in photovoltaic devices, FF quantifies the deviation of the experimental sensing curve from an ideal response profile by comparing the area enclosed by the response curve with the corresponding ideal area. Recently, this concept has also been adopted and further extended by other researchers for gas sensor evaluation, highlighting its potential as a complementary performance descriptor beyond conventional response and response/recovery time analyses [21]. Based on the response curve shown in Fig. 12(b), the calculated FF value of the VO_480 sensor is 65.34%, which falls within the "good performance" category according to the

proposed FF classification. This result indicates that the sensor exhibits not only a high response magnitude but also favorable response dynamics, supporting the overall sensing performance demonstrated by the optimized V_2O_5 nanosheet structure.

These results confirm that the VO_480 sensor not only exhibits high sensitivity but also possesses fast response–recovery characteristics, making it a promising candidate for practical NH_3 gas sensing applications. The symmetric and repeatable response–recovery cycles further indicate the excellent reliability and reproducibility of the sensor. The repeatability and long-term stability of the VO_480 sensor were evaluated through short-term cyclic measurements performed at the optimum operating temperature of 207 °C under 50 ppm NH_3 exposure. The tests were conducted during both the first week and the 24th week to assess the temporal stability of the sensor performance, as presented in Figure 13.

The dynamic response curves demonstrate highly reproducible behavior over seven consecutive sensing cycles. In each cycle, the sensor exhibits a rapid increase in sensitivity upon exposure to NH_3, followed by a consistent return to its baseline value once the gas is removed, indicating excellent reversibility.

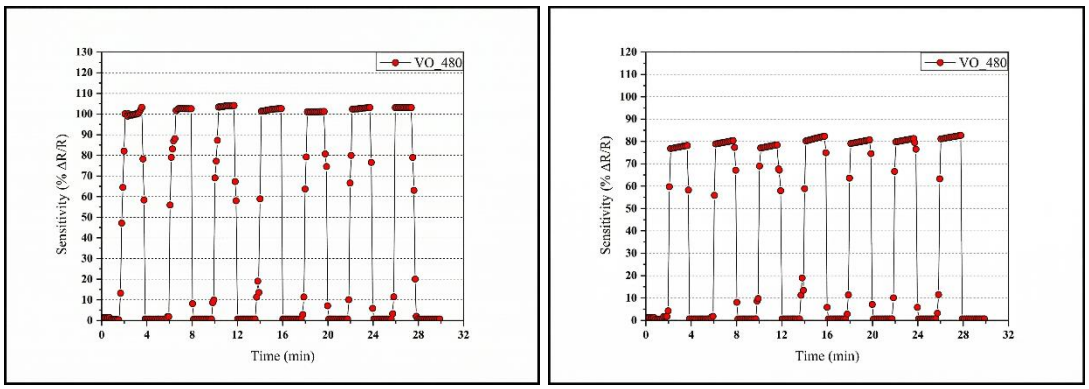


Figure 13. Short-term repeatability test results from the first week vs. short-term repeatability test results from the 24th week

Quantitatively, the variation in sensitivity between cycles was found to be approximately 3% during the first-week measurements and about 5% after 24 weeks. The slight increase in variation over time may be attributed to minor surface modifications or gradual changes in adsorption–desorption dynamics. Nevertheless, the sensor maintains a highly stable and reliable response even after prolonged operation. These results confirm that the VO_480 sensor possesses excellent repeatability and long-term stability, which are critical requirements for practical gas sensing applications. The excellent stability can be attributed to the robust nanosheet morphology and stable crystal structure of the VO_480 sample.

The chemiresistive response of VOx thin films to NH_3 is driven by a two-stage surface process: initial analyte capture mediated by the electrophilic V^{5+} Lewis acid centers, followed by oxidation of the adsorbed NH_3 through reactive surface oxygen anions with concurrent electron return to the conduction band. At the operating temperatures employed in this study (67–207 °C), surface-bound O^- anions represent the primary reactive intermediates; the Lewis acidity of V^{5+} sites facilitates preferential NH_3 coordination and orientation prior to this oxidation step [15, 16].

Under air exposure, atmospheric O_2 molecules chemisorb onto the VOx surface and extract conduction-band electrons, converting to surface-stabilized oxygen anions whose speciation depends on temperature: O_2^- prevails below approximately 100 °C, O^- dominates in the 100–300 °C window, and O^{2-} forms above 300 °C [4, 14]. Within the 67–207 °C operating range of this study, O^- is therefore the dominant ionosorbed species. Progressive electron withdrawal by these anions broadens the near-surface depletion region and raises the film resistance substantially. The sequential ionosorption steps can be represented as:

O_2 (gas) → O_2 (ads)

O_2 (ads) + e^- → O_2^- (ads)

O_2^- (ads) + e^- → $2O^-$ (ads)

Upon NH_3 admission, the analyte molecules interact with the surface-bound O^- species, returning the captured electrons to the conduction band and collapsing the depletion layer; the net outcome is a measurable decrease in film resistance. This heterogeneous oxidation can be written as:

$2NH_3 + 3O^- \rightarrow N_2 + 3H_2O + 3e^-$

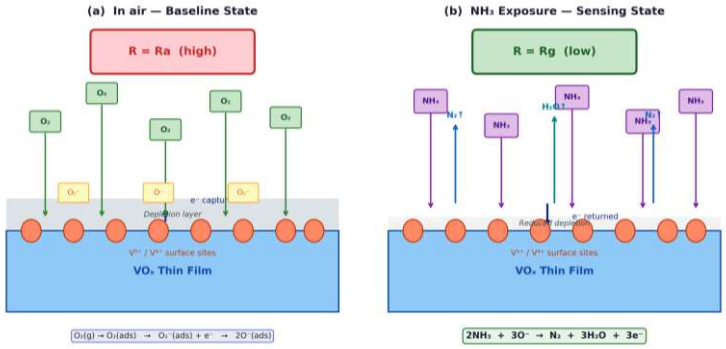


Figure 14. Schematic of the NH_3 sensing mechanism of VOx thin films. (a) In air: O_2 adsorbs on V^{5+}/V^{4+} sites forming ionized oxygen species that deplete the near-surface electron density (high resistance R_a). (b) Under NH_3 exposure: NH_3 reacts with adsorbed oxygen species, releasing electrons back to the conduction band and reducing resistance to R_g.

The magnitude of the resulting resistance shift scales with the density of O^--occupied surface sites, the total accessible adsorption sites of the film, and the efficiency of charge transport through the oxide network — all three of which are strongly modulated by the annealing-induced structural evolution documented in this work. The superior sensing performance of the VO_480 sensor can primarily be attributed to the synergistic effect of its structural and morphological characteristics. The well-crystallized orthorhombic V_2O_5 phase identified by XRD is expected to support efficient charge transport, while the porous nanosheet-like morphology observed by FESEM provides more accessible surface sites and facilitates NH_3

diffusion. In addition, V^{5+}/V^{4+} mediated surface redox reactions, widely reported for V_2O_5 based gas sensors, may also contribute to the enhanced sensing response by facilitating electron exchange during NH_3 adsorption [14–16]. Previous reports consistently attribute the enhanced NH_3 sensing performance of V_2O_5-based materials to the synergistic contribution of accessible surface-active sites and V^{5+}/V^{4+} mediated electron transfer processes, which facilitate rapid adsorption, surface oxidation, and charge exchange during gas sensing [14–18]. The formation of a nearly phase-pure orthorhombic V_2O_5 phase together with the porous nanosheet morphology is therefore expected to provide favorable conditions for these surface reactions, leading to more efficient adsorption–reaction–desorption processes. The optimized combination of crystallinity, low microstrain, and nanosheet morphology at 480 °C therefore provides favorable conditions for efficient adsorption–reaction–desorption processes, resulting in high sensitivity, rapid response–recovery behavior, and good long-term stability.

Table 6 presents a comparative evaluation of the NH_3 sensing performance of the VOx thin-film sensors developed in this study with previously reported V_2O_5 based sensing materials. Direct comparison of the reported response values should be interpreted with caution, since the literature data were obtained using different response definitions, gas concentrations, operating temperatures, and measurement protocols. As clearly seen, the sputter-deposited VOx sensors demonstrate competitive, and in several cases superior, performance compared to the literature. In particular, the VO_480 sample exhibits a remarkably high response toward NH_3 (104% at 50 ppm) while operating at a moderate temperature of 207 °C. This enhanced performance can be attributed to the synergistic effects of annealing-induced phase purification, improved crystallinity, and the formation of a porous nanosheet-like morphology, which together provide a high density of active adsorption sites and efficient charge transport pathways.

Compared with many previously reported V_2O_5-based sensors, which often require complex nanostructuring strategies, elevated synthesis temperatures, or additional functionalization (e.g., noble metal decoration), the present approach achieves strong sensing characteristics using a relatively simple and scalable reactive DC magnetron sputtering process. Furthermore, certain samples such as VO_460 demonstrate appreciable sensing performance at significantly lower operating temperatures (67 °C), highlighting the versatility of the developed system in balancing sensitivity and lower-temperature depending on application requirements. Overall, these results indicate that controlled post-annealing of sputtered VOx thin films provides an effective and practical route for enhancing NH_3 sensing performance, offering a promising alternative for low-cost, reproducible, and scalable gas sensor fabrication. This combination of high sensitivity, moderate operating temperature, and scalable fabrication makes the present VOx system highly attractive for practical NH_3 sensing applications. It should be noted that direct numerical comparison is limited by differences in response definitions, operating temperatures, gas concentrations, and measurement protocols among the reported studies.

Table 6. Studies in the literature include some V_2O_5 sensors produced with different manufacturing techniques and studies on NH_3 gas.

Sensor material	**Production Method**	**Operating Temperature (°C)**	**Concentration**	**Sensitivity**	**Response eq**	**Reference**
V_2O_5 (thin film)	Pulsed Laser Deposition	623	40-640 ppb	0.4	$S=\Delta R/R_{air}$	[22]
V_2O_5 (nanorods)	CVD	400	100 ppm	230	$S=\Delta R/R_{air}$ x100	[15]
V_2O_5 (nanoflowers)	Hydrothermal	250	100 ppm	4.5	$S=\Delta R/R_{air}$ x100	[23]

V_2O_5 (nano fibers)	Electro spin	260	100 ppb	6	$S=\Delta R/R_{air}$	[24]
V_2O_5 (nano fibers)	Sol-gel	200	2,1 ppm	11	$S=\Delta R/R_{air}$ x100	[25]
V_2O_5 (nanorods)	Hydrothermal	80	100 ppm	2.6	$S=\Delta R/R_{air}$	[26]
V_2O_5	Chemical Method	Room Temperature	500 ppm	5.5	$S=R_{gas}/R_{air}$	[27]
V_2O_5 (nanoflakes)	Hydrothermal	Room Temperature	100 ppm	67	$S=\Delta R/R_{air}$ x100	[1]
V_2O_5 (porous nanosheets)	RF Magnetron Sputtering + Nanoimprint	Room Temperature	75 ppm	17	$S=R_{air}/R_{gas}$	[28]
V_2O_5 (nanosheets)	Hydrothermal	Room Temperature	5 ppm	9.4	$S=\Delta R/R_{air}$ x100	[29]
V_2O_5 (nanoparticles)	Chemical Synthesis	Room Temperature	1 ppm	17	$S=\Delta R/R_{air}$ x100	[16]
V_2O_5 (nanoparticles)	Microwave Synthesis	Room Temperature	1 ppm	1.16	$S=R_{air}/R_{gas}$	[30]
V_2O_5 (nanosheets)	Reactive DC Magnetron Sputtering	67 (VO_460)	50 ppm	42	$S=\Delta R/R_{air}$ x100	This work
		207 (VO_480)	50 ppm	104	$S=\Delta R/R_{air}$ x100	

4. CONCLUSION

In this study, VOx thin-film NH_3 sensors were successfully fabricated via reactive DC magnetron sputtering and systematically optimized through post-deposition annealing in the temperature range of 100–550 °C. Structural and morphological analyses revealed that the as-deposited films possessed a smooth and amorphous nature, while annealing induced significant surface roughening, nanosheet/nanolayer formation (particularly ≥480 °C), and phase transformation from mixed V_3O_7/ V_2O_5 to a highly oriented orthorhombic V_2O_5 structure. XRD results confirmed progressive grain growth and decreased internal strain with increasing annealing temperature, indicating improved crystallinity and structural stability. These annealing-induced microstructural and phase modifications directly influenced the gas-sensing performance of the films. Among all samples, the VO_480 sensor exhibited the best performance, achieving a maximum response of 104% toward 50 ppm NH_3 at an operating temperature of 207 °C. Furthermore, the calculated fill factor (FF_{aqar}) of 65.34% classifies the optimized VO_480 sensor within the "good performance" category, demonstrating that the proposed FF metric can serve as a useful complementary descriptor for evaluating the dynamic behavior of chemiresistive gas sensors. This superior sensing behavior is attributed mainly to the synergistic effects of the porous nanosheet morphology, improved crystallinity, and reduced microstrain. Literature-reported V^{5+}/V^{4+} mediated surface redox processes in V_2O_5 may also contribute to the observed response. Furthermore, certain samples demonstrated appreciable sensitivity at relatively low operating temperatures, highlighting the potential for reduced-heating sensing applications. It should be noted that all measurements were performed under dry air conditions; the effects of relative humidity and cross-sensitivities to common interfering gases (e.g., CO, NO_2, H_2S) were not investigated in this work and represent important directions for future study. Overall, the results clearly demonstrate that annealing temperature is a critical parameter for tailoring the structural, morphological, and functional properties of VOx thin films. This study provides a simple, scalable, and cost-effective strategy

for the development of high-performance NH_3 gas sensors, and highlights sputtered V_2O_5 thin films as promising candidates for practical sensing applications.

5. FUNDING DECLARATION

The authors declare that no funds, grants, or other support were received during the preparation of this manuscript.

6. REFERENCE

[1] H. Yin, C. Song, Z. Wang, W. Zhang, J. Li, and Z. Wu, "Self-Assembled Vanadium Oxide Nanoflakes for p-Type Ammonia Sensors at Room Temperature," Nanomaterials, vol. 9, no. 3, p. 317, 2019. doi: 10.3390/nano9030317.

[2] D. Kwak, Y. Lei, and R. Maric, "Ammonia gas sensors: A comprehensive review," Talanta, vol. 204, pp. 713–730, 2019. doi: 10.1016/j.talanta.2019.06.034.

[3] B. Timmer, W. Olthuis, and A. van den Berg, "Ammonia sensors and their applications — a review," Sens. Actuators B Chem., vol. 107, no. 2, pp. 666–677, 2005. doi: 10.1016/j.snb.2004.11.054.

[4] C. Wang, L. Yin, L. Zhang, D. Xiang, and R. Gao, "Metal oxide gas sensors: sensitivity and influencing factors," Sensors, vol. 10, no. 3, pp. 2088–2106, 2010. doi: 10.3390/s100302088.

[5] X. Liu, N. Chen, B. Han, X. Xiao, G. Chen, I. Djerdj, and Y. Wang, "Nanoparticle cluster gas sensor: Pt activated SnO_2 nanoparticles for NH_3 detection with ultrahigh sensitivity," Nanoscale, vol. 7, no. 36, pp. 14872–14880, 2015. doi: 10.1039/C5NR03585F.

[6] G. H. Mhlongo, D. E. Motaung, F. R. Cummings, H. C. Swart, and S. S. Ray, "A highly responsive NH_3 sensor based on Pd-loaded ZnO nanoparticles prepared via a chemical precipitation approach," Sci. Rep., vol. 9, p. 9881, 2019. doi: 10.1038/s41598-019-46247-z.

[7] X. Tian, X. Cui, T. Lai, J. Ren, Z. Yang, M. Xiao, B. Wang, X. Xiao, and Y. Wang, "Gas sensors based on TiO_2 nanostructured materials for the detection of hazardous gases: A review," Nano Mater. Sci., vol. 3, no. 4, pp. 390–403, 2021. doi: 10.1016/j.nanoms.2021.05.011.

[8] H. Ji, W. Zeng, Y. Xu, Y. Li, "Nanosheet-assembled hierarchical WO_3 flower-like nanostructures: Hydrothermal synthesis and NH_3-sensing properties," Materials Letters, vol. 250, pp. 155–158, 2019. doi: 10.1016/j.matlet.2019.05.023

[9] Z. Liu, T. He, H. Sun, B. Huang, X. Li, "Layered MXene heterostructured with In_2O_3 nanoparticles for ammonia sensors at room temperature," Sensors and Actuators B: Chemical, vol. 365, art. 131918, 2022. DOI: 10.1016/j.snb.2022.131918

[10] D. Kwak, M. Wang, K. J. Koski, L. Zhang, H. Sokol, R. Maric, and Y. Lei, "α-MoO_3 nanoribbons for ultrasensitive ammonia (NH_3) gas detection: integrated experimental and density functional theory simulation studies," ACS Appl. Mater. Interfaces, vol. 11, no. 11, pp. 10697–10706, 2019. doi: 10.1021/acsami.8b20502.

[11] J. Zhou, M. Ikram, A. U. Rehman, J. Wang, Y. Zhao, K. Kan, W. Zhang, F. Raziq, L. Li, and K. Shi, "Highly selective detection of NH_3 and H_2S using the pristine CuO and mesoporous In_2O_3@CuO multijunctions nanofibers at room temperature," Sens. Actuators B Chem., vol. 255, pp. 1819–1830, 2018. doi: 10.1016/j.snb.2017.08.220.

[12] V. Amiri, H. Roshan, A. Mirzaei, and M. H. Sheikhi, "A review of nanostructured resistive-based vanadium oxide gas sensors," Chemosensors, vol. 8, no. 4, p. 105, 2020. doi: 10.3390/chemosensors8040105.

[13] N. Yamazoe, "New approaches for improving semiconductor gas sensors," Sens. Actuators B Chem., vol. 5, no. 1–4, pp. 7–19, 1991. doi: 10.1016/0925-4005(91)80213-4.

[14] V. Mounasamy, G. K. Mani, and S. Madanagurusamy, "Vanadium oxide nanostructures for chemiresistive gas and vapour sensing: a review on state of the art," Microchim. Acta, vol. 187, p. 253, 2020. doi: 10.1007/s00604-020-4182-2.

[15] A. A. Akande, T. E. Mosuang, C. N. M. Ouma, E. M. Benecha, T. Tesfamichael, K. Roro, A. G. J. Machatine, and B. W. Mwakikunga, "Ammonia gas sensing characteristics of V_2O_5 nanostructures: A combined experimental and ab initio density functional theory approach," J. Alloys Compd., vol. 821, p. 153565, 2020. doi: 10.1016/j.jallcom.2019.153565.

[16] R. P. Radhakrishnan, A. Konnola, P. R. Nair, and M. K. Jayaraj, "Spectroscopic determination of the role of vanadyl oxygen in room temperature NH_3 sensing by V_2O_5 nanoparticles," Spectrochim. Acta A, vol. 287, p. 122092, 2023. doi: 10.1016/j.saa.2022.122092.

[17] C. Batista, J. Mendes, V. Teixeira, and J. Carneiro, "Reactive DC Magnetron Sputtering of Vanadium Oxide Thin Films," Mater. Sci. Forum, vols. 587–588, pp. 343–347, 2008. doi: 10.4028/www.scientific.net/MSF.587-588.343.

[18] G. Rampelberg, K. De Keyser, B. Parmentier, K. Devloo-Casier, E. Langereis, H. C. M. Knoops, D. Deduytsche, and C. Detavernier, "Facile Phase Control of Multivalent Vanadium Oxide Thin Films (V_2O_5 and VO_2) by Atomic Layer Deposition and Postdeposition Annealing," ACS Appl. Mater. Interfaces, vol. 9, no. 26, pp. 23042–23052, 2017. doi: 10.1021/acsami.7b03398.

[19] M. Hijazi, V. Stambouli, M. Rieu, G. Tournier, J.-P. Viricelle, and C. Pijolat, "Ambient temperature selective ammonia gas sensor based on SnO_2-APTES modifications," Sens. Actuators B Chem., vol. 256, pp. 440–447, 2018. doi: 10.1016/j.snb.2017.10.036.

[20] A. Ajjaq, F. Bulut, O. Ozturk and S. Acar “Advanced NH3 Detection by 1D Nanostructured La:ZnO Sensors with Novel Intrinsic p−n Shifting and Ultra high Baseline Stability” ACS Sens, vol.10, p.7257, 2025 doi: 0.1021/acssensors.3c02256

[21] P. Wang, M. Li, Z. Zhu and C. Tang “GasSensorSelectivityAssessment Indicatorof Fill Factor from Response Curve: A Case Study on WS2-Based Ammonia Gas Sensors” ACS Sens, vol. 9, p.895, 2024 doi: 10.1021/acssensors.5c01453

[22] A. Boudiba, C. Zhang, C. Baroni, M. Debliquy, R. Snyders, and M.-G. Olivier, "Nanostructured vanadium pentoxide gas sensors for SCR process control," J. Mater. Sci., vol. 52, pp. 1871–1880, 2017. doi: 10.1007/s10853-016-0517-0.

[23] Y. Qin, G. Fan, K. Liu, and M. Hu, "Vanadium pentoxide hierarchical structure networks for high performance ethanol gas sensor with dual working temperature characteristic," Sens. Actuators B Chem., vol. 190, pp. 141–148, 2014. doi: 10.1016/j.snb.2013.08.061.

[24] V. Modafferi, S. Trocino, A. Donato, G. Panzera, and G. Neri, "Electrospun V_2O_5 composite fibers: Synthesis, characterization and ammonia sensing properties," Thin Solid Films, vol. 548, pp. 689–694, 2013. doi: 10.1016/j.tsf.2013.03.137.

[25] V. Modafferi, G. Panzera, A. Donato, P. L. Antonucci, C. Cannilla, N. Donato, D. Spadaro, and G. Neri, "Highly sensitive ammonia resistive sensor based on electrospun V_2O_5 fibers," Sens. Actuators B Chem., vol. 163, pp. 61–68, 2012. doi: 10.1016/j.snb.2012.01.007.

[26] A. D. Raj, T. Pazhanivel, P. S. Kumar, D. Mangalaraj, D. Nataraj, and N. Ponpandian, "Self assembled V_2O_5 nanorods for gas sensors," Curr. Appl. Phys., vol. 10, pp. 531–537, 2010. doi: 10.1016/j.cap.2009.07.015.

[27] S. N. Birajdar, N. Y. Hebalkar, S. K. Pardeshi, S. K. Kulkarni, and P. V. Adhyapak, "Ruthenium-decorated vanadium pentoxide for room temperature ammonia sensing," RSC Adv., vol. 9, pp. 28735–28745, 2019. doi: 10.1039/C9RA04382A.

[28] V. Mounasamy, G. K. Mani, K. Tsuchiya, and S. Madanagurusamy, "Nanoimprint assisted free standing porous vanadium oxide nanosheet based ammonia sensor," Appl. Surf. Sci., vol. 541, p. 148271, 2021. doi: 10.1016/j.apsusc.2020.148271.

[29] L. V. Duy, T. T. Nguyet, D. T. T. Le, N. V. Duy, H. Nguyen, F. Biasioli, M. Tonezzer, C. Di Natale, and N. D. Hoa, "Room temperature ammonia gas sensor based on p-type-like V_2O_5 nanosheets towards food spoilage monitoring," Nanomaterials, vol. 13, no. 1, p. 146, 2023. doi: 10.3390/nano13010146.

[30] N. D. P. Nam, D. T. Huong, P. H. Anh, B. X. Hoang, L. H. Phuoc, N. T. Nghi, L. K. Hoang, D. D. Vuong, and V. X. Hien, "Microwave-synthesized V_2O_5 nanoparticles for ammonia sensing at room temperature," Mater. Sci. Eng. B, vol. 307, p. 117533, 2024. doi: 10.1016/j.mseb.2024.117533.